The terminal velocity of volcanic particles with shape obtained from 3D X-raymicrotomography

Fabio Dioguardi[1], Daniela Mele[2], Pierfrancesco Dellino[2], Tobias Dürig[3]

[1] British Geological Survey, The Lyell Centre, Edinburgh, United Kingdom

[2] University of Bari, Dipartimento di Scienze della Terra e Geoambientali, Bari, Italy

[3] University of Iceland, Institute of Earth Sciences, Reykjavik, Iceland

Corresponding author: Dr. Fabio Dioguardi, PhD. Email: fabiod@bgs.ac.uk

Abstract

New experiments of falling volcanic particles were performed in order to defineterminal velocity models applicable in a wide range of Reynolds number*Re*. Experiments were carried out with fluids of various viscosities andwith particles that cover a wide range of size, density and shape. Particle shape, which strongly influencesfluid drag, was measured in 3D by High-resolution X-Ray microtomography, by whichsphericityΦ_{3D} and fractal dimensionD_{3D}were obtained. They are easier to measure and less operator dependent than the 2D shape parameters used in previous papers. Drag laws that make use of the new 3D parameters were obtained by fitting particle data to the experiments, andsingle-equation terminal velocity models were derived. They work well both at high and low Re($3x10^{-2}<Re< 10^4$), while earlierformulationsmade use of different equations at different ranges of *Re*. The new drag lawsare well suited for the modellingof particle transportation both in the eruptive column, where coarse and fine particles are present,andalso in the distal part of the umbrella region,where fine ash isinvolved in the large-scale domains of atmospheric circulation.A table of the typical values of $\Phi_{3D}$and D_{3D} of particles from known plinian, subplinian and ash plume eruptions is presented.Graphs of terminal velocity as a function of grain size are finally proposed as tools to help volcanologists and atmosphere scientiststo model particle transportationof explosive eruptions.

Keywords: 3D sphericity; 3D fractal dimension; particle shape;fluid drag; X-Ray Micro-tomography;terminal velocity

1. Introduction

Terminal velocity w_t is used for modelling the transportation and sedimentation of particulate material in multiphaseflows (Stow and Bowen, 1980; Bonadonna et al., 2005; Pfeiffer et al., 2005; Costa et al., 2006; Jones et al., 2007; Barsotti et al., 2008;Folch et al., 2008; Dellino et al., 2008;Alfano et al., 2011; Bonadonna et al., 2012; Sulpizio et al., 2012;Devenish 2013;Dioguardi et al., 2014; Dioguardi and Dellino, 2014; Beckett et al., 2015;de' MichieliVitturi et al, 2015;Doronzo et al. 2015;Cerminara et al., 2016; Costa et al., 2016). It is defined by Newton's impact law:

$$w_t = \sqrt{\frac{4(\rho_p - \rho_f) g d_p}{3 C_d \rho_f}} \quad (1)$$

where g is the gravitational acceleration, d_p and ρ_p are particle size and density, and ρ_f is fluid density (see Table 1 for notation). C_d is the drag coefficient, which is a functionof both particle Reynolds number, $Re = \frac{\rho_f w_t d_p}{\mu_f}$, where μ_f is fluid viscosity, and of particle shape S. In order to predict terminal velocity, a law that defines the dependency of C_d on both Re and S is needed. Volcanic particles show a very wide range of shapes, which are difficult to describe by simple geometric forms(Dellino and La Volpe 1996; Dürig et al. 2012; Jordan et al. 2014; Leibrandt and Le Pennec 2015; Vonlanthen et al. 2015).To dateshape descriptorshave been based on various combinationsof 2D parameters.For examplethe approximatesphericity Φ, which is one of the most widely used parametersin drag laws(Wilson and Huang (1979); Haider and Levenspiel (1989); Swamee and Ojha (1991);Ganser (1993); Chien (1994); Pfeiffer et al. (2005); Hölzer and Sommerfeld (2008);Bagheri and Bonadonna (2016)), is defined by:

$$\Phi = \frac{A_{sph}}{A_p} = \frac{\sqrt[3]{(6V_p)^{\frac{2}{3}}}}{A_p} \qquad (2)$$

where A_{sph} is the surface area of the sphere equivalent to the particle of volume $V_p$and A_p is the particle surface area, which is calculated by approximating the particleto a simple non-spherical smooth shape (e.g. scalene ellipsoid: Dellino et al. 2005; Bagheri et al. 2015; Liu et al. 2015). There actually exist some optical instruments that allow a fast semiautomatic measurement of the average value of sphericity of a particle population dispersed in a fluid(e.g. RetschCAMSIZER and Malvern Morphologi G3), but if one needs precise measurements onindividual particles, data are not readily available by such instrumentations. Measurements on individual particles are needed when falling particle experiments are to be used to define drag laws. In order to obtainmeasurements of sphericity on a particle, the three perpendicular axes of the scalene ellipsoid approximating the particle can be measured by image processing analysis on high-resolution photographs of particles mounted on a goniometric stage taken under astereomicroscope(Dellino et al., 2005). The method is not trivial and expertise is needed for orienting particles in order to get significant and stable measurements, which makes the procedure far to be automatic and strongly operator dependent (Bagheri et al., 2015; Liu et al., 2015).With this method, in fact, in order to measure the three principal axes, the particle has to be positioned in a way that the maximum projection section can be captured, from which the maximum and minimum axis can be measured. Subsequently, the particle has to be rotated orthogonallyfor measuring the intermediate axis (Dellino et al., 2005). Given the highly irregular shape of volcanic particles, errors in the identification of the maximum projection section cannot be avoided, which thenpropagate into the measurement of the three axes. In addition, by this method shape is derivedby a combination of measurements made on 2D images, which does not allow taking into full account all the 3Dsurface irregularities of glassy volcanic particles. Finally, approximating the particle surface area A_p to that of simple, yet non-spherical solids leads to an underestimation of the actual value of A_p, which unavoidably affect the interpretation of drag measurement of irregular rough particles.

Another shape parameter frequently used for particulate materialscomes from the fractal theory, which defines a fractal as an object whose shape is scale-independent (Mandelbrot, 1977). If L is the length of the fractal line approximating the contour of the object with ever-decreasing segments of length scale s, the following equation holds:

$$L = ks^{-D} \tag{3}$$

Where D is the fractal dimension and k is a number. Graphically D is the slope of the line in the plot log(L) vs. log(s). Fractal analysis has been widely used in engineering for different purposes, for example for correlating fractal dimension of particles tosoil bulk properties(e.g. Arasan et al. 2010). In volcanology, the 2D fractal characteristics of ash particles have been associated to the fragmentation processes of explosive eruptions(Dellino and Liotino, 2002; Kueppers et al. 2006; Perugini et al., 2011; Rausch et al., 2015), but to our knowledge, it has not been applied yet for the characterization of particle drag in fluids.

In this paper, we take advantage of X-ray microtomographyas to quantifythe true tridimensionalshape characteristics of a collection of volcanic particles from a number of known explosive eruptions. With the aim of deriving drag laws based on our new shape parameters, the particleswereused in falling experiments,by which terminal velocity data were obtained from video analysis. The drag laws have been tested against other formulations available in the literature and used for drawing charts of terminal velocity as a function of particle size for particles of representative volcanic eruptions. These serve as a reference for volcanologists who want to get first estimates of terminal velocity without the use of more or less complex modelling.

Material and methods

a) 3Dparticle-shape characterization

We selected a set of volcanic particles based on two requirements:

1) they had to span over a wide range of size, morphology and density guaranteeing an ample variation of both C_d and *Re* when used in falling experiments;

2) they had to come from tephra layers of a number of explosive eruptions, thus representing a significant range of textural properties ofparticles originating from different types of magma, volcanoes, fragmentation and transport processes.

Particles were sampled from the juvenile glass component of:1) Eyjafjallajökull2010 (Dellino et al., 2012) and Grímsvötn(Jude-Etonet al. 2012)subplinianeruptionsof basaltic composition in Iceland (Eyjaf and Grim in Figure 2);2) Avellino3900 BP (PAV)Plinian eruption (Sulpizio et al., 2010)and Pollena472 AD (Pol)subplinian eruption(Sulpizio et al., 2005) of tephritic-phonolitic composition of Vesuvius, the latter coming from pyroclastic density currents deposits;3) Agnano Monte-Spina 4500 BP (AMS) Plinian eruption (de Vita et al., 1999) of trachytic composition of CampiFlegrei;4) 2001ADash plumes of basaltic composition of Etna (Scollo et al., 2007) (Etna). In the case of Avellino, particles were collected both from the Plinian fallout deposits of the first phase of the eruption (PAV_{fall})and from the pyroclastic density currents deposits that were emplaced during the final phase of the eruption (PAV_{PDC}) (Sulpizio et al., 2010). This choice was made as to check the difference in shape, and in terminal velocity, of particles produced during different phases of a large eruption.

A set of 127 particles was so formedof which size, density and shape weremeasured. A subset had been already used in previous papers (Dellino et al., 2005; Dioguardi and Mele, 2015).It has been included here for comparing results of the present research with earlier ones.

For 3D particle-shapeanalysis,we useda Bruker Skyscan 1172 high-resolution μX-CT scanner (MCT). The system is equipped with a polychromatic micro focus X-ray tube, characterized by a maximum operating voltage of 100 kV and a maximum output power of 10 W. The minimum detectable dimension is 0.5 μm. In the instrument, a particle is placed in front of an X-ray beam and is rotated stepwise. Different projections are acquired by collecting transmitted X-rays with a sensitive CCD camera. Raw data are reconstructed into two-dimensional cross-sections (slices) by application of the FDK algorithm (Feldkamp et al., 1984; Kak and Stanley, 1988). In this study,the pixel sizewas chosen as to achieve a constant image area of the slices of 400000 px^2,so to obtain size-independent parameters (Dellino and La Volpe, 1996; Mele et al., 2011) and reproducible results once the operating conditions are held constant. In Table 2 all the size-dependent operating conditions with the μX-CT scanner are listed.From interpolation of the 2D slices,a 3D model of the object is constructed. In digital imaging, the passage from 2D to 3D implies a change from a digital bi-dimensional representation of an object by means of a discrete number of equal-sized elements called pixels to a digital tri-dimensional representation by means of a discrete number of equal-sized cubes called voxels.By the 3D model, with an analysis of the voxels distribution,a number of morphological characteristics of the objectcan be extracted.We used the MCT to extract particle size, volume, and the 3D shape descriptors sphericity Φ_{3D} and fractal dimension D_{3D}.

Sphericity $\Phi_{3D}$was obtained byusing, in equation (2),as particle volume the number of all the voxels enclosing the particle, times the volume of one voxel. Surface areacalculation wasbased on the isosurface surrounding the object voxels,with each voxel exposing a surface obtained byan interpolation algorithmworking on the marching cube method (Lorensen and Cline, 1987).

The fractal dimension$D_{3D}$was implemented as an extension of the 2D method described in the previous section.An algorithm based on the“box counting” methodwas used(e.g. Chappard et al. 2001),by which the 3D digital objectwas divided into an array of equal-sized cubes, which were counted. The procedure was repeated over a range of cube sizes, and the number of cubes was plotted against cube size in a log-log plot. As for 2D contours, the 3D fractal dimension (D_{3D}) is the slope of the regression line.

Particle size was obtained by the diameter of the volume of the equivalent sphere. It ranged from 0.17 to 11.04 mm.

Particle density was obtained by considering the volume as obtained by MCT and mass as determined by precision balances, it ranged from1.245 to 3.284 g cm^{-3}.

The Sheet “Experiments and fittings” in the Excel file “Data_experiments_models.xlsx”available in the folder Supplementary Material contains all the particles properties (size, density, shape, etc.), experiments, calculations and fitting analysis results. Data show that our volcanic particles have highly variable morphologies. Φ_{3D} ranges from 0.065 to 0.732, while D_{3D} from 2.027 to 2.565. It is to note that the lower the sphericity, the more particle shape is irregular (being Φ_{3D} = 1 for a perfect sphere), while the opposite occurs to D_{3D}(being D_{3D} = 2 for a perfect sphere),and the two parameters are very well inversely correlated(Figure 1). This is an important result meaning that D_{3D} can be used for characterizing 3D particle shape in the same manner as sphericity, which is the most widely used shape parameter for characterizing the aerodynamic drag of particles. Furthermore, the correlation between fractal dimension and other shape parameters has already been described (e.g. Arasan et al., 2011). Fractal dimension D_{3D} shows less dispersed data compared to sphericityΦ_{3D}, having a lower percentage of variation (standard deviation/average value)among particles of the same eruption (see Table 3).

A closer look at Figure 2 shows how the distribution of particle surface irregularities, which strongly affects the shape descriptors, varies in the eruptions under study, and is strongly influenced by the size and number of vesicles (gas bubbles). The basaltic compositions,namely Etna2001(Figure 2a), and Iceland, (Figure 2b and c) show a few coarser sub-spherical vesicles that result in less irregular surfaces, hence a higher sphericity $\Phi_{3D}$and a lower fractal dimensionD_{3D}. In addition, the particles coming from pyroclastic density current deposits of the Avellino eruption at Vesuvius show a small amount of vesicles (Figure 2d), with high Φ_{3D} and low D_{3D}.A similar behaviour is visible for the pyroclastic density current particles of the Pollena eruption at Vesuvius (Figure 2e).The trachytic particles of Plinian fallout deposits of CampiFlegrei (Figure 2f) and of the phonolitic-tephritic Plinian fallout deposits of the Avellino eruption at Vesuvius (Figure 2g) have a much higher amount of tiny stretched vesicles intertwined with small crystals that render highly irregular the clast surface, with the sphericityΦ_{3D}being relatively low and fractal dimension D_{3D}high. Table3shows that particle density is lower for the CampiFlegrei sample and for the Plinian fallout of Avellino; whereas it is higher for both Etna and Iceland and also for the pyroclastic density currents of Pollena and Avellino. Particle density depends both on magma composition and on the amount of gas bubbles. The dense rock equivalent density (ρ_{DRE}) is the measure of the bubble free density, which is solely related to magma composition. By comparing ρ_{DRE} to particle density in Table 3, it is possible to get an idea of the influence of vesicularity on particle density. In fact, Avellino particles coming from fallout and pyroclastic density currents, which have the samevalue of ρ_{DRE} (they come from the same magma composition),have quite different particle densities, lower for the Plinian fallout, higher for the pyroclastic density current. The difference is due to the different amount of vesicles, which in turn influences also particle shape (Liu et al., 2015). Therefore,vesicularity has a double effect on particles; itproduces an increase of particle surface irregularity and a decrease ofparticle density, both playing a role on particle drag and terminal velocity,which analysis is the focus of next section.

b) Falling particle experiments

The fluid-particle drag was quantified by measuring the terminal velocity of each particle falling throughout fluids. Three different fluids of known density and viscosity were used: distilled water; a solution of 60% glycerol and 40% distilled water; and a solution of 86.5% distilled water and 13.5% glycerol.Water-glycerol solutions have a viscosity that is a function of both glycerol concentration and temperature, which is calculated by the online calculator based on the parametrisation of Cheng (2008) (Reading viscosity calculator). Temperature was constantly monitored with a thermometer with 0.2 °C accuracy (which resulted in an uncertainty in the fluid viscosity calculation up to 0.5% and up to 0.01% for fluid density, for the most glycerol-rich solution). By using the three solutions and by changing temperature, viscosity ranged between 0.009 and 1.647 P and density between 0.997 and 1.235 g cm^{-3}.Some particles were experimented with all three fluids, resulting in a total number of 275 experimental runs.

Particle trajectories were monitored by using high-resolution video cameras with a spatial resolution of 1920 x 1080 pixels for the experiments with glycerol-water solution (cylinder of height of 30 cm and inner radius 5 cm) and 1280 x 720 pixels for experiments in water, for which a longer cylinder(height of 1.5 m and inner radius of 5 cm) was used to ensure the particles reached their terminal velocity.

All videos were recorded at 25 fps and the frames featured a spatial resolution of typically ~11 pixels/mm. Particle terminal velocity was obtained by measuring the space travelled by the particle $z$and dividing it by the time interval Δt, which is the product of the frame rate times the number of frames, after the particle reached a constant falling velocity. The number of frames varied from experiment to experiment, and were specifically adjusted to keep the uncertainty onw_t always below 5%. For example, in cases of very low terminal velocities, the spatial uncertaintyΔz might reach the order of the displacement z itself. For these cases a large measuring frame interval of 100 frames (i.e., Δt= 4s) had to be chosen.On the other hand, particles with a high terminal velocity would be too fast for such large measuring intervals, but since in these cases $\Delta z << z$, also considerably smaller frame intervals could be used (down to 5), resulting in still significantly low uncertainties for w_t.

The drag coefficient was calculated by inverting the terminal velocity equation (1) and isolating $C_{d,meas}$:

$$C_{d,meas} = \frac{4(\rho_p - \rho_f) g d_p}{3 \rho_f w_t^2} \qquad (4)$$

All the measured terminal velocities and drag coefficientsare listed in the Sheet “Experiments and fittings” in the Excel file “Data_experiments_models.xlsx” available in the Supplementary Material folder.

On Figure3 the $C_d$vs.Re diagram is shown,where all the experimental runs ($C_{d,meas}$)are plotted (black circles).Re ranges from $3*10^{-2}$ to about $5*10^3$while $C_{d,meas}$covers a rangefrom $6.2*10^{-1}$ to $2.4*10^3$. For each experimental point we recalculated the drag coefficient of the sphere$C_{d,sphere}$ at the corresponding Re number by applying the formula of Clift and Gauvin (1971) (grey circles):

$$C_{d,sphere} = \frac{24}{Re}(1 + 0.15Re^{0.687}) + \frac{0.42}{1 + \frac{42500}{Re^{1.16}}} \quad for\ Re < 3\ \times 10^5 \qquad (5)$$

Although the trends look similar, the experimental data points are shifted toward higher values compared to spheres at the same *Re*, meaning that the shape irregularities of volcanic particles increase the C_d compared to that of spheres. The difference in C_d between our particles and spheres is much higher at higher *Re*, while it is smaller, but still significant, at lower *Re* where turbulence around particles is less pronounced. This is not surprising and in agreement with theoretical studies and previous experimental observations (Ganser 1993; Dellino et al., 2005; Dioguardi and Mele, 2015; Bagheri and Bonadonna, 2016).

Modelling and discussion

In order to model particle terminal velocity and the transport of discrete particles in multiphase flows, a drag law of the form $C_d = f(Re, S)$ is needed.It was searched by fitting falling particle experiments to particle characteristics. For making the search simpler, some mathematical manipulation is needed in order to let the lefthand side of the equation be independent of terminal velocity. In fact, C_d and *Re* are both dependent on terminal velocity. To circumvent the problem, as proposed byDellino et al. (2005) and Dioguardi and Mele (2015), C_d was multiplied by the squared Reynolds number:

Thus the quantity C_dRe^2

$$C_dRe^2 = \frac{4(\rho_p - \rho_f)g\rho_f d_p^3}{3\mu_f^2} \qquad (6)$$

is independent fromterminal velocity.

To further simplify, the approach of Dietrich (1982),who made use of the Archimedes number*Ar*, is applied:

$$Ar = \frac{(\rho_s - \rho_f)\rho_f g}{\mu_f^2} d_p^3 \qquad (7)$$

By rearranging (6) and (7), the following relationship holds:

$$C_d Re^2 = \frac{4}{3} Ar \qquad (8)$$

Weknow from Figure3 that the drag coefficient of our volcanic particles $C_{d,meas}$is influenced by particle shape. We then introduced a shape descriptor *S*that allowedtaking into account shape irregularity. With this aim, in (8)$C_d$is substituted with$C_{d,sphere}$:,

$$Ar = \frac{3}{4} C_{d,sphere} Re^2 \qquad (9)$$

The shape parameter *S* is finally included into the final form of the drag law and we searched for a fitting of the type $Ar/C_{d,sphere} = f\left(Re^{exp1} S^{Re_p^{exp2}}\right)$, where we left the possibility for the exponent of *Re* to be different from 2 and the exponent of the shape parameter *S*to be*Re*-dependent, which is in agreement with our observation that the influence of the particle shape depends on *Re* (Figure 3). From preliminary analyses, it became evident that the best fit was represented by a power law:

$$\frac{Ar}{C_{d,sphere}} = a\left(Re^{exp1} S^{Re_p^{exp2}}\right)^b \qquad (10)$$

S is replaced alternatively by the sphericity $\Phi_{3D}$and fractal dimension D_{3D} in order to obtain the drag law for each shape descriptors. It is worth noting that, due to the opposite dependency of the shape descriptors on the particle irregularity (the more irregular the particle, the higher D_{3D} and the lower Φ_{3D}), the exponent of S should be positive when considering D_{3D} and negative when considering Φ_{3D}. Consequently, the correlation laws are:

$$\frac{Ar}{C_{d,sphere}} = a\left(Re^{exp1} D_{3D}^{Re_p^{exp2}}\right)^b \tag{11a}$$

$$\frac{Ar}{C_{d,sphere}} = a\left(Re^{exp1} \Phi_{3D}^{-Re_p^{exp2}}\right)^b \tag{11b}$$

By substituting Ar with $\frac{3}{4} C_d Re^2$ (eq. 8), the equations for C_d can be readily obtained:

$$C_d = \frac{4}{3} \frac{a C_{d,sphere} \left(Re^{exp1} D_{3D}^{Re_p^{exp2}}\right)^b}{Re^2} \tag{12a}$$

$$C_d = \frac{4}{3} \frac{a C_{d,sphere} \left(Re^{exp1} \Phi_{3D}^{-Re_p^{exp2}}\right)^b}{Re^2} \tag{12b}$$

By means of a Matlabcode, the values of *exp1* and *exp2* that allowed the best fit with both sphericity $\Phi_{3D}$and fractal dimension D_{3D}were iteratively searched. In each iteration, the code calculated a and $b$for each shape descriptor in (11a) or (11b) and recalculated the drag coefficient for all the particles in the database, $C_{d,rec}$ by means of (12a) or (12b), respectively. With these values, the terminal velocities of the particles were recalculated by substituting (12a) or (12b) in (1). The recalculated terminal velocities$w_{t,rec}$ were compared to the measured ones ($w_{t,meas}$) and a linear fit of the type $y = mx$,where $w_{t,rec}$ is y and the experimentally measured velocity$w_{t,meas}$ is x,was searched by the least square method. The selected exponentswere the ones that resulted in the maximum correlation coefficient of the linear fitting and the minimum difference between m and 1 (as $y=x$ would mean $w_{t,rec}= w_{t,meas}$).

Figure4 a and b show the best fittings, which were obtained,for the fractal dimension D_{3D} formulawith $exp1$ = 1.62,and $exp2$ = -0.13(Figure 4a); while for sphericity $\Phi_{3D}$$exp1$ = 4.18; $exp2$ = -0.2(Figure 4b). The correlation coefficient is very high for both shape descriptors, with the fractal dimension D_{3D}showing a little better performance (less scatter) in fitting data at very low Re.

By substituting the values of a and$b$ of the best fittings and of the exponents, the drag formulas were finally obtained:

$$C_d = \frac{4}{3}\frac{0.3492 C_{d,sphere}\left(Re^{1.62} D_{3D}^{Re^{-0.13}}\right)^{1.3358}}{Re^2} \tag{13a}$$

$$C_d = \frac{4}{3}\frac{0.559 C_{d,sphere}\left(Re^{4.18} \Phi_{3D}^{-Re^{-0.2}}\right)^{0.5134}}{Re^2} \tag{13b}$$

By means of the drag laws the C_d of the particles of our databasewere recalculated ($C_{d,rec}$)and plotted on Figure5 (a for D_{3D}, b for Φ_{3D})where the trends of $C_{d,rec}$are compared with those of the measured drag coefficients$C_{d,meas}$ and of spheres at corresponding Re, $C_{d,sphere}$. $C_{d,rec}$is always shifted toward higher values compared to spheres.In both cases the difference is much higher at high Re, where turbulence is more strongly influenced by surface irregularities, being about 200%at Re=5000.Even at very low Re the difference, while lower,is still significant (about 50%), meaning that also when turbulence intensity is not high, particle shape still influences fluid drag. The shift is clearer with the fractal dimension,which has a smaller data scatter (Figure 5).

By including the drag laws (13a)or(13b) in equation (1), the terminal velocity of all experiments was recalculated ($w_{t,rec}$) separately for the case of sphericity Φ_{3D} and of fractal dimension D_{3D}. Figure6 shows the diagram of $w_{t,rec}$ vs.$w_{t,meas}$ for the case offractal dimension D_{3D} (Figure 6a) and of sphericity Φ_{3D}(Figure 6b). The fitting is always good, with a correlation coefficient of 0.998 for $D_{3D}$and 0.984 for $\Phi_{3D}$and the recalculatedvelocitieslay around the equality line, with the slope of the correlation line being practically equal to one. This means that by our new drag laws it is possible to predict the terminal velocity of volcanic particles with confidence, both at high and low *Re*. Data points at very low *Re* are better fitted by means of the drag law that includes the fractal dimensionD_{3D} as it can be inferred by comparingFigure 6a with 6b.

For thesubsetof particles that had been used also in previous papers, the values of the approximate sphericity (as obtained with the method exposed in the introduction section) and of “shape factor” Ψas defined by Dellino et al. (2005)were available, together with sphericity $\Phi_{3D}$and fractal dimension D_{3D} (see “Comparison” and “Only-shape” sheets in the Excel file “Data_experiments_model” included in the Supplementary Material folder). On this subset, the terminal velocity was recalculated by means of: the drag laws of Chien (1984),Ganser (1993), which make use of approximate sphericity Φ; the drag lawof Dioguardi and Mele (2015), which make use of the shape factor as defined by Dellino et al. (2005); our new drag laws that make use of Φ_{3D} andD_{3D}.As it is shown on Figure 7,all the laws have a good fitting but our ones, which are based on3D shape descriptors, have a little higher correlation coefficient and lay exactly on the equality line between calculated and measured velocities (slope = 1) (Figure 7d and e). In particular, the Chien and Ganser law (Figure 7a and b respectively), which are among the most widely used,have a lower correlation coefficient and also the slope is a little bit different than 1. The difference can be better explained by inspecting theintercomparison*Cd-Re*diagram where data recalculated both with our drag laws and with those of Chien and Ganser are plotted (Figure 8). The Chien and Ganser laws have a higher data scatter, especially at high *Re*.It is not surprising, since the two laws were not designed for modelling the behaviour of coarse particles, which is important in the case of volcanic multiphase flows thatinvolve both coarse and fine particles. The root mean squares of residuals between measured and calculated data is in fact higher for Chien (RMS = 3.072) and Ganser (RMS = 2.828) laws compared to ours, with the fractal dimension D_{3D} (RMS = 2.58; RMS = 1.93 for the complete dataset) performing a little better than Φ_{3D}(RMS= 2.45; RMS = 1.84 for the complete dataset). The Dioguardi and Mele(2015) drag law (Figure 7c) has a performance similar to our ones (RMS = 2.393), but it uses a step function for switching parameters when passing from high tolow *Re* (at a value of 50).This feature complicates the implementation of the drag law inside numerical codes that model the transport of volcanic particles a bit, with some convergence issues when *Re* approaches the switching value. Our new laws, instead, are defined by a single equation,which is easy to implement in a numerical code and does not have the aforementioned convergence issues.

In order to show the typical settling velocityof particles from known explosive eruptions, on Figure9 terminal velocity curves as a function of grain size are shown (9a for the model with D_{3D}, 9b for the model with Φ_{3D}). The particle size is shown here in φ units ($\varphi = -\log_2 d_p$). For the calculation of curves, the average values of density and particle shape of each eruption,as reported in Table 3, were used. It is to note that, as terminal velocity is a function of C_d, which is a function of both *Re* and $C_{d,sphere}$ (see eq. 1 and 13), and as *Re* in turn is a function of the terminal velocity itself, an iterative procedure is needed for calculating w_t. The procedure is simple and easy to include in numerical models. It is implemented in the Matlab code wt_calculator.m and FORTRAN code wt_calculator.f included in the Supplementary material/Terminal_velocity_calculation folder, together with a short explanation of the iterative procedure (“Terminal velocity calculation.docx”).

The Reynolds-number contoursare also plotted (dotted lines),in order to show how the velocity curves diverge as the *Re* increase.At higher *Re*, the difference in terminal velocity is much higher,as shape irregularities more strongly influence the turbulence structure around particles. Twogroupsof curves, which define two types of particles that have similar velocities, and similar vesicle amount and densities, can be observed.Type 1 includeshighly vesiculated, low density, particles from the Plinian fallouts of Avellino (PAV_{fall}; Sulpizio et al., 2010) and Agnano Monte-Spina (AMS; de Vita et al., 1999), which have a lower terminal velocity; Type 2 includesmoderately vesicular, high density, particles from Avellino (PAV_{PDC}; Sulpizio et al., 2010)and Pollena (Pol; Sulpizio et al., 2005) pyroclastic density currents, plusEyjafjallajökull (Eyja; Dellino et al., 2010),Grímsvötn (Grim; Jude-Eaton et al., 2012) and Etna (Etna; Scollo et al., 2007)particles, which have a higher terminal velocity. The difference in terminal velocity of these two types of particles are quite significant.If one considers the curve of type 1compared with those oftype 2 particles, the difference in velocity for a -3 phi (8 mm)particle is about 250 cm s^{-1}. Care must be taken when considering particle density: in order to draw these charts, particle density has been considered to be constant for all the investigated dimension range, which may not be the case especially for vesiculated and crystal-rich pyroclasts.

At low*Re* the difference is relatively smaller, but it is still significant as it is shown by an inspection of the zoomed plots on the right. For example, with a size of 6phi (16 µm), the difference is about 1 cm s^{-1}. The difference in particle terminal velocity between the two graphs referring to Φ_{3D} and D_{3D} are not substantial, and are more pronounced at low *Re*. In that case, we suggest the use of the drag law that makes use of fractal dimension D_{3D}, which we know has a better fitting at lower *Re*.

In the diagramsof Figure 9also the curve of spheres with densities similar to that of the two types of particles are shown, to see how large is the difference in terminal velocity betweenactual volcanic particles and perfect spheres. As expected, the density increases as *Re* (hence particle size) increases, but it is still not negligible at very low *Re* (less than 0.01).

The big difference of terminal velocity that emerges whencomparing particlesof different eruptions suggests that, for modelling purposes, not only it is important to have a precise drag law but also precise data on size, shape and density. We demonstrate that such particle characteristics,which influence terminal velocity, are strongly dependent on the amount and size of gas bubbles.They not only change between one eruption and the other, but also can change during the different phases of a large explosive eruption.Such is the case of Avellino where the Plinian fallout phase is due to magmatic fragmentation of a vesicle rich magma; while the phase that formed pyroclastic density currents was fed by a phreatomagmatic fragmentation mechanism acting on a vesicle poor magma (Sulpizio et al., 2010). It is therefore mandatory to have good data on particles when modelling the transportation and deposition of explosive eruptions.

Conclusive remarks

The use of micro-tomographic techniques allowed thedescription of volcanic particles by the tridimensional shape parameters sphericity $\Phi_{3D}$and fractal dimensionD_{3D}, which are less operator dependent and easier to measure than 2D descriptors used in drag laws of previous studies.Particles were used in falling experiments,which allowed constructing drag laws valid both at high and low *Re*. This guarantees the applicability of our new lawsfor a wide range of conditions occurring in explosive eruptions, which span from the transportation in the eruptive column, which is rich both in coarse and fine particles, and also in the distal part of the umbrella region of Plinian eruptions, where very fine ash is involved in the large scale domain of atmosphere circulation.On this account, while the smaller scatter of data at low

*Re*makesthe fractal dimension D_{3D}particularly useful for very fine particles, we do not discard the utility of sphericity, which has been already largely used in the literature for deriving shape dependent drag laws. The 3D implementation of sphericity Φ_{3D} represents an improvement for the morphologial characterization of irregularly shaped particles. In addition, there already exist instruments allowing a semiautomatic measurement of the average values of tridimensional sphericity of ash samples, which would render quite easy to self-tailor terminal velocity calculation by means of our drag law.

We think that our drag laws can be useful also for other engineering and environmental applications, besides volcanology. In fact, with the new drag laws, the terminal velocity of irregularly shaped particulate material can be predicted by means of a single-equation model, that simplifies the implementation in numerical codes.For this purpose, in the auxiliary material the numerical code for the modelling of terminal velocity is included.

Precise data on particle characteristics are needed for obtaining realistic values of terminal velocities, andwe are conscious that devices as MCT are not available to all volcanologists and atmosphere scientists involved in the modelling of volcanic processes. Data of Table3 and graphs of Figure9 represent abasic source of information onthe typical values of shape, density and terminal velocity of particles of a number of known explosive eruptions.In the future we prospect a systematic study of particles from other volcanoes, in order to increase the database. We do not expect, however, a much bigger range of variation of shape parameters with respect to whatobtained in the present study.

Acknowledgements

Bruker Skyscan 1172 high-resolution μX-CT scanner has been purchased with funds from "PON Ricerca e Competitivitá 2007-2013".

We wish to thank Dr. Karoly Nemeth and an anonymous reviewer for their valuable comments.

Published with permission of the Executive Director of British Geological Survey (NERC)

References

Alfano, F., Bonadonna, C., Delmelle, P., Costantini, L. (2011): Insights on tephra settling velocity from morphological observations, J. Volcanol. Geotherm. Res. 208, 86-98, doi:10.1016/j.jvolgeores.2011.09.013.

Arasan, S., Yener, E., Hattatoglou, F., Akbulut, S., Hinislioglu, S. (2010): The relationship between the fractal dimension and mechanical properties of asphalt concrete, Int. J. Civ. Struct. Eng. 1, 165-170, doi:10.6088/ijcser.00202010014.

Arasan, S., Akbulut, S., Hasiloglu, A.S. (2011): The relationship between the fractal dimension and shape properties of particles, KSCE J. Civ. Eng. 15(7), 1219-1225, doi:10.1007/ s12205-011-1310-x.

Bagheri, G.H., Bonadonna, C., Manzella, I., Vonlanthen, P. (2015): On the characterization of size and shape of irregular particles, Powder Technol. 270, 141-153, doi:10.1016/j.powtec.2014.10.015.

Bagheri, G.H., Bonadonna, C. (2016): On the drag of freely falling non-spherical particles, Powder Technol. 301, 526-544, doi:10.1016/j.powtec.2016.06.015.

Barsotti, S., Neri, A., Scire, J.S. (2008): The VOL-CALPUFF model for atmospheric ash dispersal: 1. Approach and physical formulation, J. Geophys. Res. 113, B03208, doi:10.1029/2006JB004623.

Beckett, F.M., Witham, C.S., Hort, M.C., Stevenson, J.A., Bonadonna, C., Millington S.C. (2015): Sensitivity of dispersion model forecasts of volcanic ash clouds to the physical characteristics of the particles, J. Geophys. Res. Atmos. 120, 11636 – 11652, doi:10.1002/2015JD023609.

Bonadonna, C., Connor, C.B., Houghton, B.F., Connor, L., Byrne, M., Laing, A., Hincks, T., (2005): Probabilistic modeling of tephra dispersion: hazard assessment of a multi-phase eruption at Tarawera, New Zealand, J. Geophys. Res. 110, B03203.

Bonadonna, C., Genco, R., Gouhier, M., Pistolesi, M., Cioni, R., Alfano, F., Hoskuldsson, A., Ripepe, M. (2011): Tephra sedimentation during the 2010 Eyjafjallajökull eruption (Iceland) from deposit, radar, and satellite observations, J. Geophys. Res. 116, B12, doi:10.1029/2011JB008462.

Bonadonna, C., Folch, A., Loughlin, S., Puempel, H. (2012): Future developments in modelling and monitoring of volcanic ash clouds: outcomes from the first IAVCEI-WMO workshop on Ash Dispersal Forecast and Civil Aviation, Bull. Volcanol. 74, 1-10, doi:10.1007/s00445-011-0508-6.

Cerminara, M., EspostiOngaro, T., Berselli, L.C. (2016): ASHEE-1.0: a compressible, equilibrium–Eulerian model for volcanic ash plumes, Geosci. Model Dev. 9, 697–730, doi:10.5194/gmd-9-697-2016.

Chappard, D., Legrand, E., Haettich, B., Chales, G., Auvinet, B., Eschard, J.P., Hamelin, J.P., Basle, M.F., Audran, M. (2001): Fractal dimension of trabecular bone: comparison of three histomorphometric computed techniques for measuring the architectural two-dimensional complexity, J. Pathol.195, 515-521. doi:10.1002/path.970.

Cheng N. (2008): Formula for the Viscosity of a Glycerol−Water Mixture, Ind. Eng. Chem. Res., 47(9), 3285–3288, doi:10.1021/ie071349z.

Chien, S.F. (1994): Settling velocity of irregularly shaped particles, SPE Drill. Complet. 9, 281–288.

Clift R., Gauvin W.H. (1971): Motion of entrained particles in gas streams, Can. J. Chem. Eng. 49(4), 439-448.

Costa, A., Macedonio, G., Folch, A. (2006): A three-dimensional Eulerian model for transport and deposition of volcanic ashes, Earth Planet. Sci. Lett. 241, 634–647, doi:10.1016/j.epsl.2005.11.019.

Costa, A., Suzuki, Y.K., Cerminara, M., Devenish B.J., Esposti Ongaro, T., Herzog, M., et al. (2016): Results of the eruptive column model inter-comparison study, J. Volcanol. Geotherm. Res. In press, doi:10.1016/j.jvolgeores.2016.01.017.

de Vita, S., Orsi, G., Civetta, L., Carandente, A., D'Antonio, M., Di Cesare, T., Di Vito, M.A., Fisher, R.V., Isaia, R., Marotta, E., Ort, M., Pappalardo, L., Southon, J. (1999): The Agnano-Monte Spina eruption in the densely populated, restless Campi Flegrei caldera (Italy), J. Volcanol. Geotherm. Res. 91, 269–301.

de' MichieliVitturi, M., Neri, A., Barsotti, S. (2015): PLUME-MoM 1.0: A new integral model of volcanic plumes based on the method of moments, Geosci. Model Dev. 8, 2447-2463, doi:10.5194/gmd-8-2447-2015.

Dellino, P., La Volpe, L. (1996): Image processing analysis in reconstructing fragmentation and transportation mechanisms of pyroclastic deposits. The case of Monte Pilato-RoccheRosse eruptions, Lipari (Aeolian Islands, Italy), J. Volcanol. Geotherm. Res. 71, 13–29. doi:10.1016/0377-0273(95)00062-3.

Dellino, P., Liotino, G. (2002): The fractal and multifractal dimension of volcanic ash particles contour: a test study on the utility and volcanological relevance, J. Volcanol. Geotherm. Res. 113, 1-18, doi:10.1016/S0377-0273(01)00247-5

Dellino, P., Mele, D., Bonasia, R., Braia, G., La Volpe, L., Sulpizio, R. (2005): The analysis of the influence of pumice shape on its terminal velocity, Geophys. Res. Lett. 32, L21306, doi:10.1029/2005GL023954.

Dellino, P., Mele, D., Sulpizio, R., La Volpe, L., Braia, G. (2008): A method for the calculation of the impact parameters of dilute pyroclastic density currents based on deposit particle characteristics, J. Geophys. Res. 113, B07206, doi:10.1029/2007JB005365.

Dellino, P, Gudmundsson, M.T., Larsen, G., Mele D., Stevenson, J.A., Thordarson, T., Zimanowski, B. (2012): Ash from the Eyjafjallajökull eruption (Iceland): fragmentation processes and aerodynamic behaviour, J. Geophys. Res. 117, doi:10.1029/2011JB008726.

Devenish, B.J. (2013): Using simple plume models to refine the source mass flux of volcanic eruptions according to atmospheric conditions, J. Volcanol. Geotherm. Res. 256, 118-127, doi:10.1016/j.jvolgeores.2013.02.015.

Dietrich, W.E. (1982): Settling velocity of natural particles, Water Resour. Res. 18(6), 1615-1626, doi:10.1029/WR018i006p01615.

Dioguardi, F., Dellino, P. (2014): PYFLOW: A computer code for the calculation of the impact parameters of Dilute Pyroclastic Density Currents (DPDC) based on field data, Comput. Geosci. 66, 200-210, doi:10.1016/j.cageo.2014.01.013.

Dioguardi, F., Dellino, P., Mele, D. (2014): Integration of a new shape-dependent particle–fluid drag coefficient law in the multiphase Eulerian–Lagrangian code MFIX-DEM, Powder Technol. 260, 68-77, doi:10.1016/j.powtec.2014.03.071

Dioguardi, F., Mele, D. (2015): A new shape dependent drag correlation formula for non-spherical rough particles. Experiments and results, Powder Technol. 277, 222-230. doi:10.1016/j.powtec.2015.02.062.

Doronzo, D.M., Khalaf, E.A., Dellino, P., de Tullio, M.D., Dioguardi, F., Gurioli, L., Mele, D., Pascazio, G., Sulpizio, R. (2015): Local impact of dust storms around a suburban building in arid and semi-arid regions: numerical simulation examples from Dubai and Riyadh, Arabian Peninsula, Arab. J. Geosci. 8: 7359, doi:10.1007/s12517-014-1730-2.

Dürig, T., Mele, D., Dellino, P., Zimanowski, B. (2012): Comparative analyses of glass fragments from brittle fracture experiments and volcanic ash particles, Bull. Volcanol. 74(3), 691-704, doi:10.1007/s00445-011-0562-0.

Feldkamp, L.A., Davis, L.C., Kress, J.W. (1984): Practical conebeam algorithm, J. Opt. Soc. Am., A1, 612–619.

Folch, A., Cavazzoni, C., Costa, A., Macedonio, G. (2008): An automatic procedure to forecast tephra fallout, J. Volcanol. Geotherm. Res. 177, 767-777, doi:10.1016/j.jvolgeores.2008.01.046.

Ganser, G.H. (1993): A rotational approach to drag prediction of spherical and nonspherical particles, Powder Technol. 77, 143–152, doi:10.1016/0032-5910(93)80051-B.

Haider, A., Levenspiel, O. (1989): Drag coefficient and terminal velocity of spherical and nonspherical particles, Powder Technol. 58, 63-70, doi:10.1016/ 0032-5910(89)80008-7.

Heap, M.J., Vinciguerra, S., Meredith, P.G. (2009): The evolution of elastic moduli with increasing crack damage during cyclic stressing of a basalt from Mt. Etna volcano, Tectonophysics 471(1), 153-160, doi:10.1016/j.tecto.2008.10.004.

Hölzer, A., Sommerfeld, M. (2008): New simple correlation formula for the drag coefficient of non-spherical particles, Powder Technol. 184, 361–365, doi:10.1016/j.powtec.2007.08.021.

Jones, A.R., Thomson, D.J., Hort, M., Devenish, B. (2007): The U.K. Met Office's next-generation atmospheric dispersion model, NAME III, in Borrego C. and Norman A.-L. (Eds) *Air Pollution Modeling and its Application XVII* (Proceedings of the 27th NATO/CCMS International Technical Meeting on Air Pollution Modelling and its Application), Springer, pp. 580-589.

Jordan, S. C., Dürig, T., Cas, R.A.F., Zimanowski, B. (2014): Processes controlling the shape of ash particles: Results of statistical IPA, J. Volcanol. Geotherm. Res. 288, 19-27, doi:10.1016/j.jvolgeores.2014.09.012

Jude-Eton, T.C., Thordarson, T., Oddsson, B. (2012): Dynamics, stratigraphy and proximal dispersal of supraglacial tephra during the ice-confined 2004 eruption at Grímsvötn Volcano, Iceland, Bull. Volcanol. 74(5), 1057-1082.

Kak, A.C., Slaney, M. (1988): Principles of Computerized Tomographic Imaging. IEEE Press, New York, pp.329.

Kueppers, U., Perugini, D., Dingwell, D.B. (2006): "Explosive energy" during volcanic eruptions from fractal analysis of pyroclasts, Earth Planet. Sci. Lett. 248(3), 800–807, doi:10.1016/j.epsl.2006.06.033.

Leibrandt, S., Le Pennec, J. L. (2015): Towards fast and routine analyses of volcanic ash morphometry for eruption surveillance applications, J. Volcanol. Geotherm. Res.297, 11-27, doi:10.1016/j.jvolgeores.2015.03.014

Liu, E.J., Cashman, K.V., Rust, A.C. (2015): Optimising shape analysis to quantify volcanic ash morphology, Geo. Res. J. 8, 14-30, doi:10.1016/j.grj.2015.09.001.

Lorensen, W.E., Cline, H.E. (1987): Marching cubes: a high resolution 3d surface construction algorithm, Comput. Graph. 21(4): 163-169.

Mandelbrot, B.B. (1977): Fractals: Form, Chance and Dimension. W.H. Freeman, San Francisco, pp. 361.

Mele, D., Dellino, P., Sulpizio, R., Braia, G. (2011): A systematic investigation on the aerodynamics of ash particles, J. Volcanol. Geotherm. Res. 203(1), 1-11, doi:10.1016/j.jvolgeores.2011.04.004.

Perugini, D., Speziali, A., Caricchi, L., Kueppers, U. (2011): Application of fractal fragmentation theory to natural pyroclastic deposits: insights into volcanic explosivity of the

Valentano scoria cone (Italy), J. Volcanol. Geotherm. Res. 202(3), 200–210, doi:10.1016/j.jvolgeores.2011.02.008.

Pfeiffer, T., Costa, A., Macedonio, G. (2005): A model for the numerical simulation of tephra fall deposits, J. Volcanol. Geotherm. Res. 140, 273–294, doi:10.1016/j.jvolgeores.2004.09.001.

Rausch, J., Grobéty, B., Volanthen, P. (2015): Eifel maars: Quantitative shape characterization of juvenile ash particles (Eifel Volcanic Field, Germany), J. Volcanol. Geotherm. Res. 291, 86-100. doi:10.1016/j.jvolgeores.2014.11.008.

Scollo, S., Del Carlo, P., Coltelli, M., (2007): Tephra fallout of 2001 Etna flank eruption: Analysis of the deposit and plume dispersion, J. Volcanol. Geotherm. Res. 160, 147–16.

Stow, D.A.V., Bowen A. J. (1980): A physical model for the transport and sorting of fine-grained sediment by turbidity currents, Sedimentology 27, 31-46.

Sulpizio, R., Mele, D., Dellino, P., La Volpe, L. (2005): A complex, Subplinian-type eruption from low-viscosity, tephri-phonolitic magma: the Pollena eruption of Somma-Vesuvius (Italy), Bull. Volcanol. 67, 743-767.

Sulpizio, R., Cioni, R., Di, Vito M.A., Mele, D., Bonasia, R., Dellino, P., La Volpe, L. (2010): The Pomici di Avellino eruption of Somma-Vesuvius (3.9 ka BP) part I: stratigraphy, compositional variably and eruptive dynamics, Bull. Volcanol. 72, 539-558, doi:10.1007/s00445-009-0339-x.

Sulpizio, R., Folch, A., Costa, A., Scaini, C., Dellino, P. (2012): Hazard assessment of far-range volcanic ash dispersal from a violent Strombolian eruption at Somma-Vesuvius volcano, Naples, Italy: implications on civil aviation, Bull. Volcanol. 74, 2205-2218, doi:10.1007/s00445-012-0656-3.

Swamee, P.K., Ojha, C.P. (1991): Drag coefficient and fall velocity of nonspherical particles, J. Hydraul. Eng. 117, 660–669, doi:10.1061/(ASCE)0733-9429(1991)117:5(660).

Vonlanthen, P., Rausch, J., Ketcham, R. A., Putlitz, B., Baumgartner, L. P., & Grobéty, B. (2015). High-resolution 3D analyses of the shape and internal constituents of small volcanic ash particles: the contribution of SEM micro-computed tomography (SEM micro-CT), J. Volcanol. Geotherm. Res.293, 1-12. doi:10.1016/j.jvolgeores.2014.11.016.

Wilson, L., Huang, T. (1979): The influence of shape on the atmospheric settling velocity of volcanic ash particles, Earth Planet. Sci. Lett. 44, 311-324.

Figure captions

Figure 1. D_{3D}vs. Φ_{3D} scatter diagram. Values of the two 3D shape parameter highly correlate each other, meaning that fractal dimension can be used for characterizing aerodynamic drag of irregular particles as well as sphericity.

Figure 2.3D surface rendering of selected particles from samples from different representative eruptions. For each particle, the scale and the values of D_{3D} and Φ_{3D} are provided. **a. Etna**: 2001 AD ash plumes of basaltic composition of Etna (Scollo et al., 2007). **b. Grim**: Grímsvötn 2004 AD eruption (Jude-Etonet al. 2012). **c. Eyjaf**: Eyjafjallajökull 2010 AD eruption (Dellino et al., 2012). **d. $\mathbf{PAV_{PDC}}$**: Avellino 3900 BP Plinian eruption (Sulpizio et al., 2010), pyroclastic density current deposit. **e. Pol**: Pollena 472 AD subplinian eruption (Sulpizio et al., 2005). **f. AMS**: 4500 BP Plinian eruption (de Vita et al., 1999). **g: $\mathbf{PAV_{fall}}$**: Avellino 3900 BP Plinian eruption (Sulpizio et al., 2010), fallout deposit.

Figure 3.C_d vs. Re diagram. Black circles represent the measured values, $C_{d,meas}$, while grey circles are the corresponding drag values for a sphere, $C_{d,sphere}$.

Figure 4. Scatter diagram of $Ar/C_{d,sphere}$vs. $Re^{exp1}S^{Re\wedge exp2}$. The solid black line represents the best power law fit, the power law function and the correlation coefficients are also

reported.**a.**$Ar/C_{d,sphere}$vs. $Re^{1.62}D_{3D}^{Re\wedge-0.13}$ scatter diagram. **b.** $Ar/C_{d,sphere}$vs. $Re^{4.18}\Phi_{3D}^{-Re\wedge-0.2}$ scatter diagram.

Figure 5. C_d vs. Re diagrams for measured drag coefficients ($C_{d,meas}$, grey circles), drag coefficient recalculated with our drag laws (eq. 13) ($C_{d,rec}$, black squares), drag coefficient of spheres at corresponding Re ($C_{d,sphere}$, grey diamonds). **a.** Diagram for the drag law with D_{3D} (eq. 13a). **b.** Diagram for the drag law with Φ_{3D} (eq. 13b).

Figure 6. $w_{t,rec}$ vs. $w_{t,meas}$ scatter diagrams. Dashed black line represent perfect agreement, solid black line is the trend line of the best linear regression, with null intercept. The values of the slope and of the correlation coefficients are displayed. In both cases the slope is nearly equal to 1 and the correlation coefficient is high. **a.** Diagram for the drag law with D_{3D} (eq. 13a). **b.** Diagram for the drag law with Φ_{3D} (eq. 13b).

Figure 7. $w_{t,rec}$ vs. $w_{t,meas}$ scatter diagrams for the reduced dataset with 2D shape descriptors. Dashed black line represent perfect agreement, solid black line is the trend line of the best linear regression, with null intercept. The values of the slope and of the correlation coefficients are displayed. **a.** Chien (1994). **b.** Ganser (1993). **c.** Dioguardi and Mele (2015). **d.** Our law in this work with D_{3D}. **e.** Our law in this work with Φ_{3D}.

Figure 8. C_d vs. Re diagrams for measured drag coefficients (clack circles), drag coefficient recalculated with our drag law with D_{3D} (eq. 13a) (purple squares), with our drag law with Φ_{3D} (eq. 13b), with Chien (1994) (green squares), with Ganser (1993) (blue triangle) and drag coefficient of spheres (black dash).

Figure 9. w_t vs. d_p(in φ units) for particles whose density and shape are representative of the samples listed in Table 3 and shown in Figure 2.Dashed line and dash and dot lines represent spheres with density of 1.4 g cm^{-3} and 2.2 g cm^{-3}, respectively. The dotted lines are contour

of particle Reynolds number *Re*. **a.** With the drag law with D_{3D} (eq. 13 a). **b**. With the drag law with D_{3D} (eq. 13 b). In each figure, the plot on the right represent a zoom for $5\varphi < d_p < 8\varphi$.

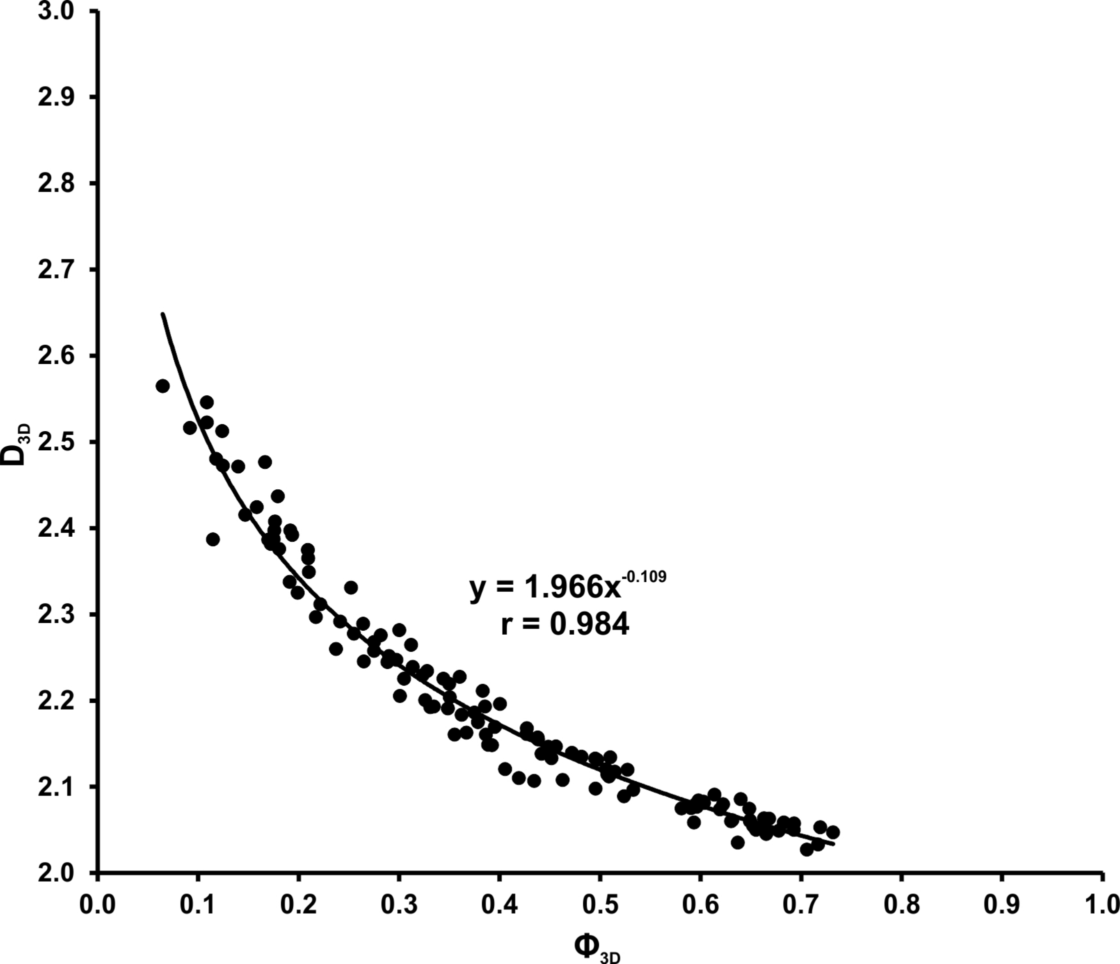

3.0
2.9
2.8
2.7
2.6
2.5
2.4
2.3
2.2
2.1
2.0
D_{3D}
y = 1.966x^-0.109
r = 0.984
0.0
0.1
0.2
0.3
0.4
0.5
0.6
0.7
0.8
0.9
1.0
Φ_{3D}

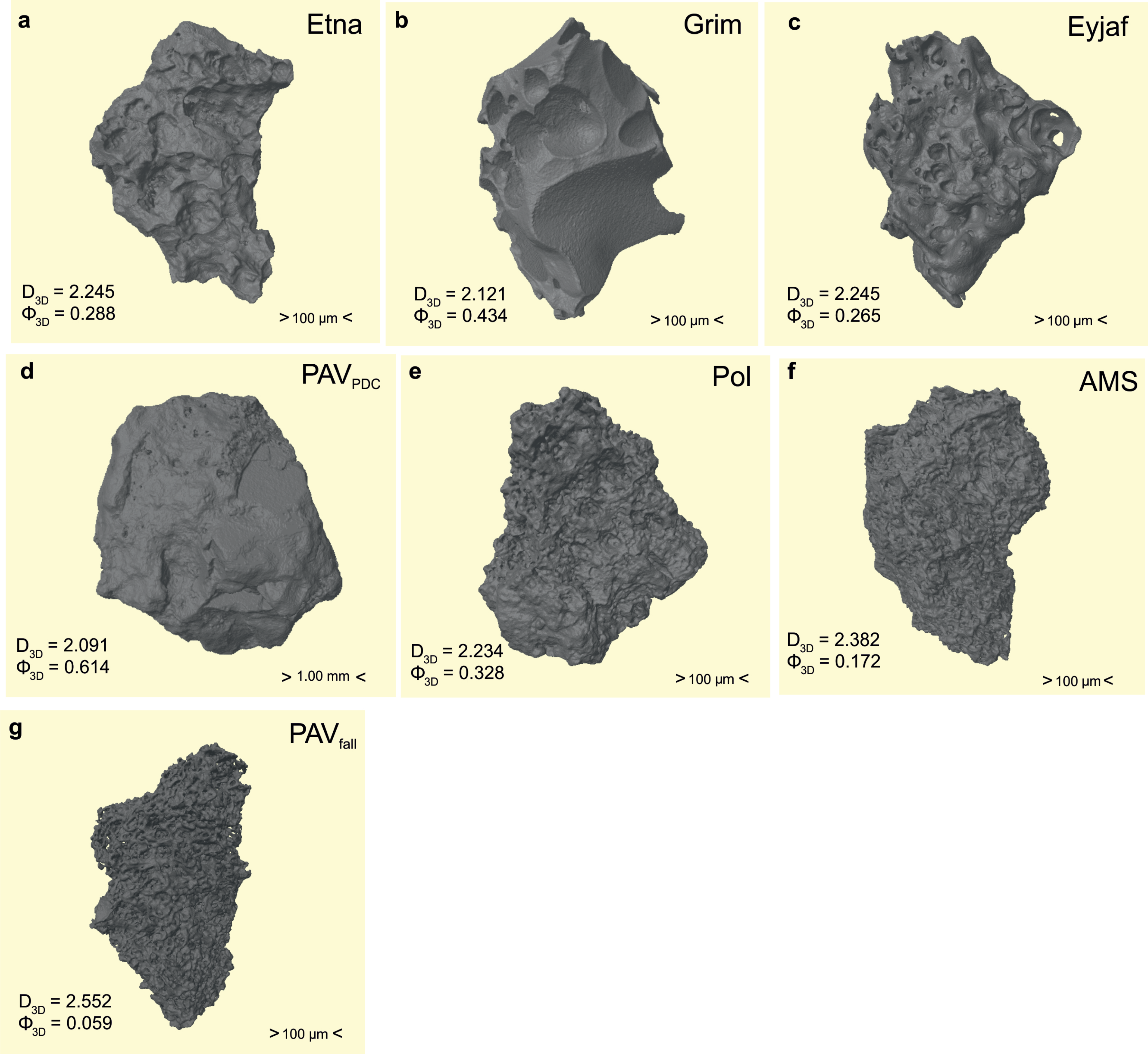
a
Etna
D3D = 2.245
Φ3D = 0.288
> 100 μm <
b
Grim
D3D = 2.121
Φ3D = 0.434
> 100 μm <
c
Eyjaf
D3D = 2.245
Φ3D = 0.265
> 100 μm <
d
PAVPDC
D3D = 2.091
Φ3D = 0.614
> 1.00 mm <
e
Pol
D3D = 2.234
Φ3D = 0.328
> 100 μm <
f
AMS
D3D = 2.382
Φ3D = 0.172
> 100 μm <
g
PAVfall
D3D = 2.552
Φ3D = 0.059
> 100 μm <

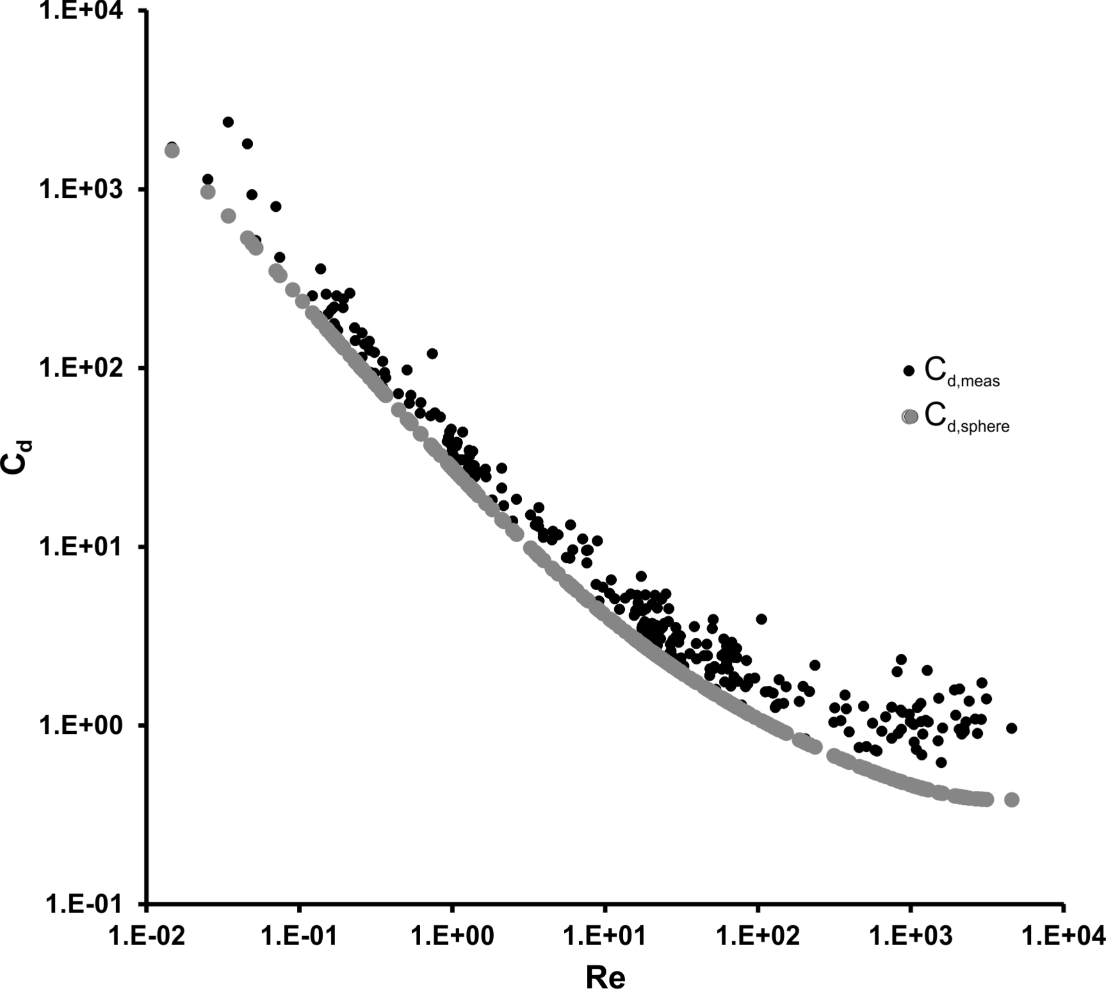
1.E+04
1.E+03
1.E+02
1.E+01
1.E+00
1.E-01
Cd
1.E-02
1.E-01
1.E+00
1.E+01
1.E+02
1.E+03
1.E+04
Re
Cd,meas
Cd,sphere

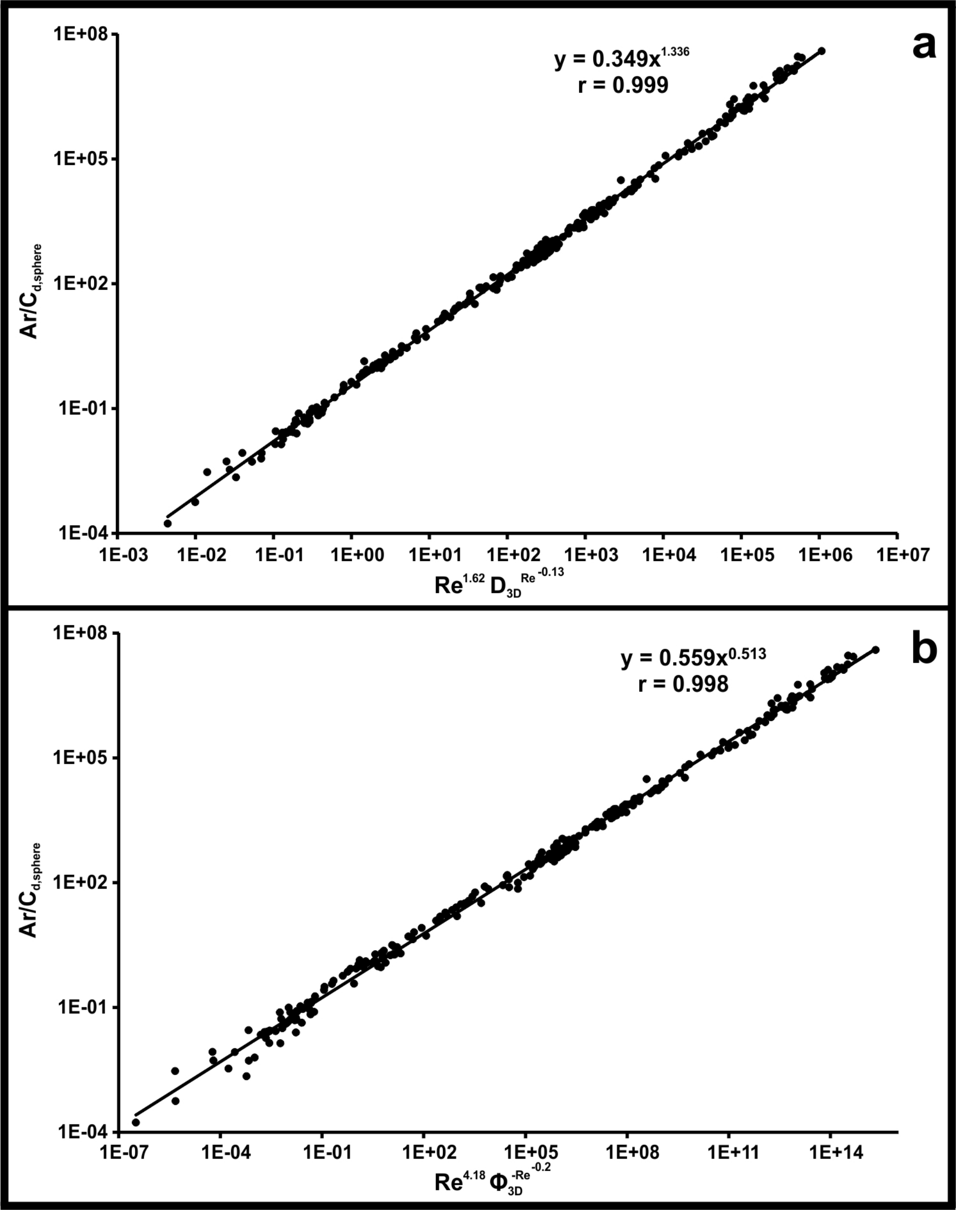
a
y = 0.349x^1.336
r = 0.999
Ar/C_d,sphere
Re^1.62 D_3D^Re^-0.13
1E+08
1E+05
1E+02
1E-01
1E-04
1E-03
1E-02
1E-01
1E+00
1E+01
1E+02
1E+03
1E+04
1E+05
1E+06
1E+07
b
y = 0.559x^0.513
r = 0.998
Ar/C_d,sphere
Re^4.18 Φ_3D^-Re^-0.2
1E+08
1E+05
1E+02
1E-01
1E-04
1E-07
1E-04
1E-01
1E+02
1E+05
1E+08
1E+11
1E+14

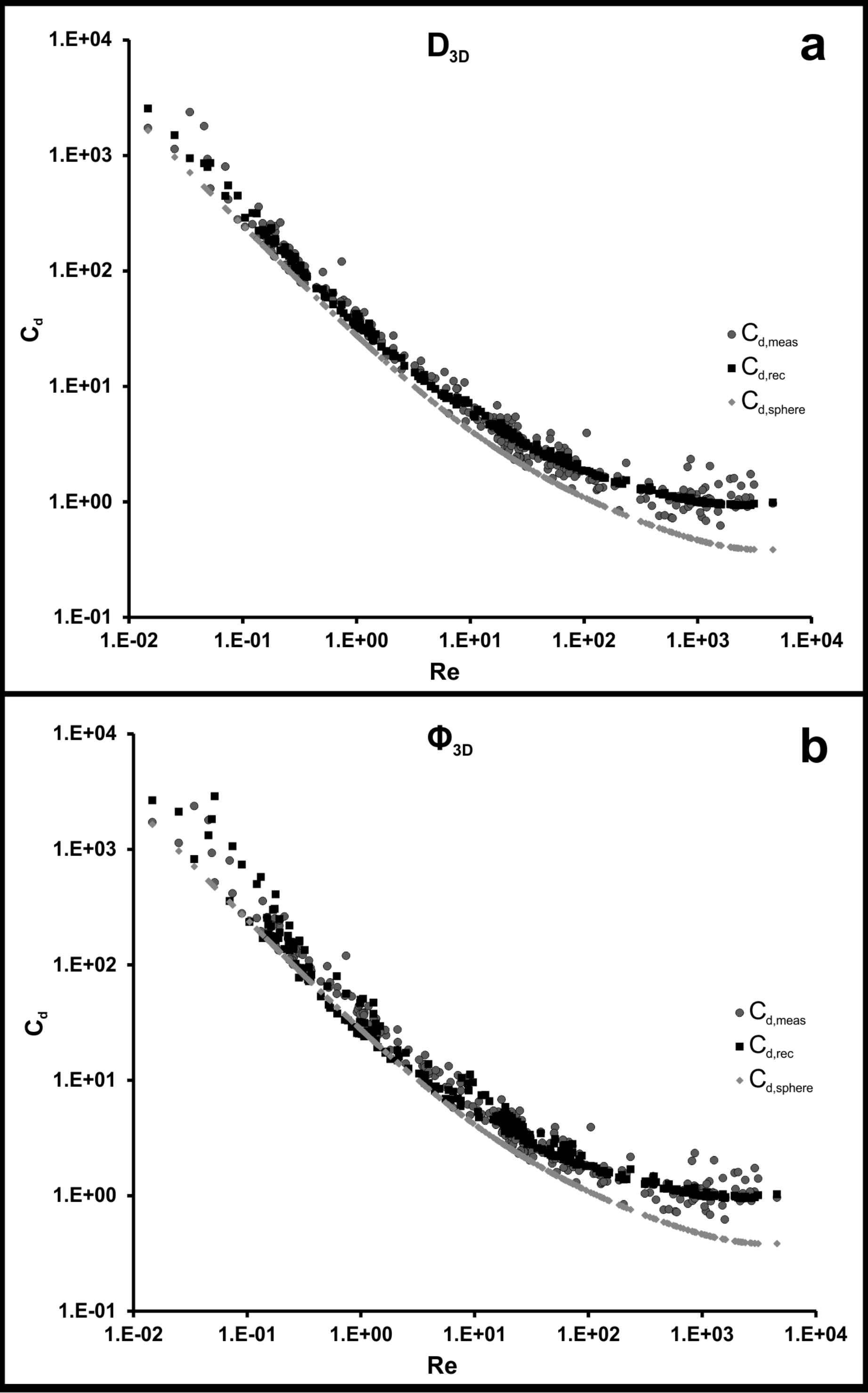
D3D
a
Cd
Re
Cd,meas
Cd,rec
Cd,sphere
1.E+04
1.E+03
1.E+02
1.E+01
1.E+00
1.E-01
1.E-02
1.E-01
1.E+00
1.E+01
1.E+02
1.E+03
1.E+04
Φ3D
b
Cd
Re
Cd,meas
Cd,rec
Cd,sphere

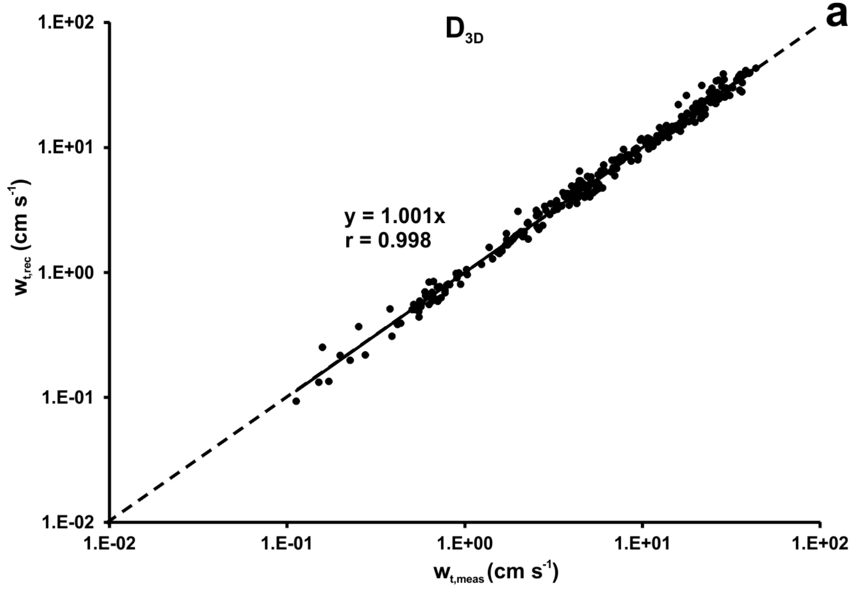
a
D3D
y = 1.001x
r = 0.998
1.E+02
1.E+01
1.E+00
1.E-01
1.E-02
1.E-02
1.E-01
1.E+00
1.E+01
1.E+02
wt,rec (cm s-1)
wt,meas (cm s-1)

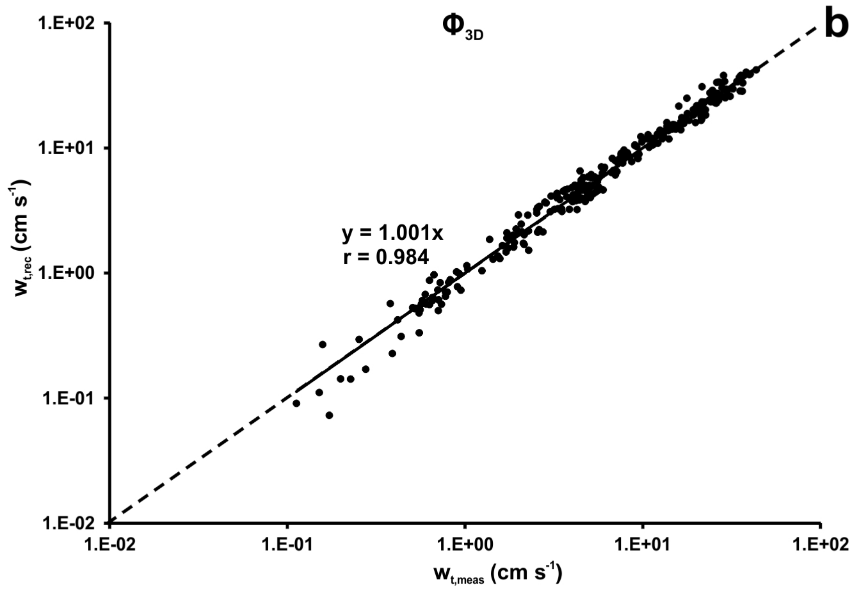
b
Φ3D
y = 1.001x
r = 0.984
1.E+02
1.E+01
1.E+00
1.E-01
1.E-02
1.E-02
1.E-01
1.E+00
1.E+01
1.E+02
wt,rec (cm s-1)
wt,meas (cm s-1)

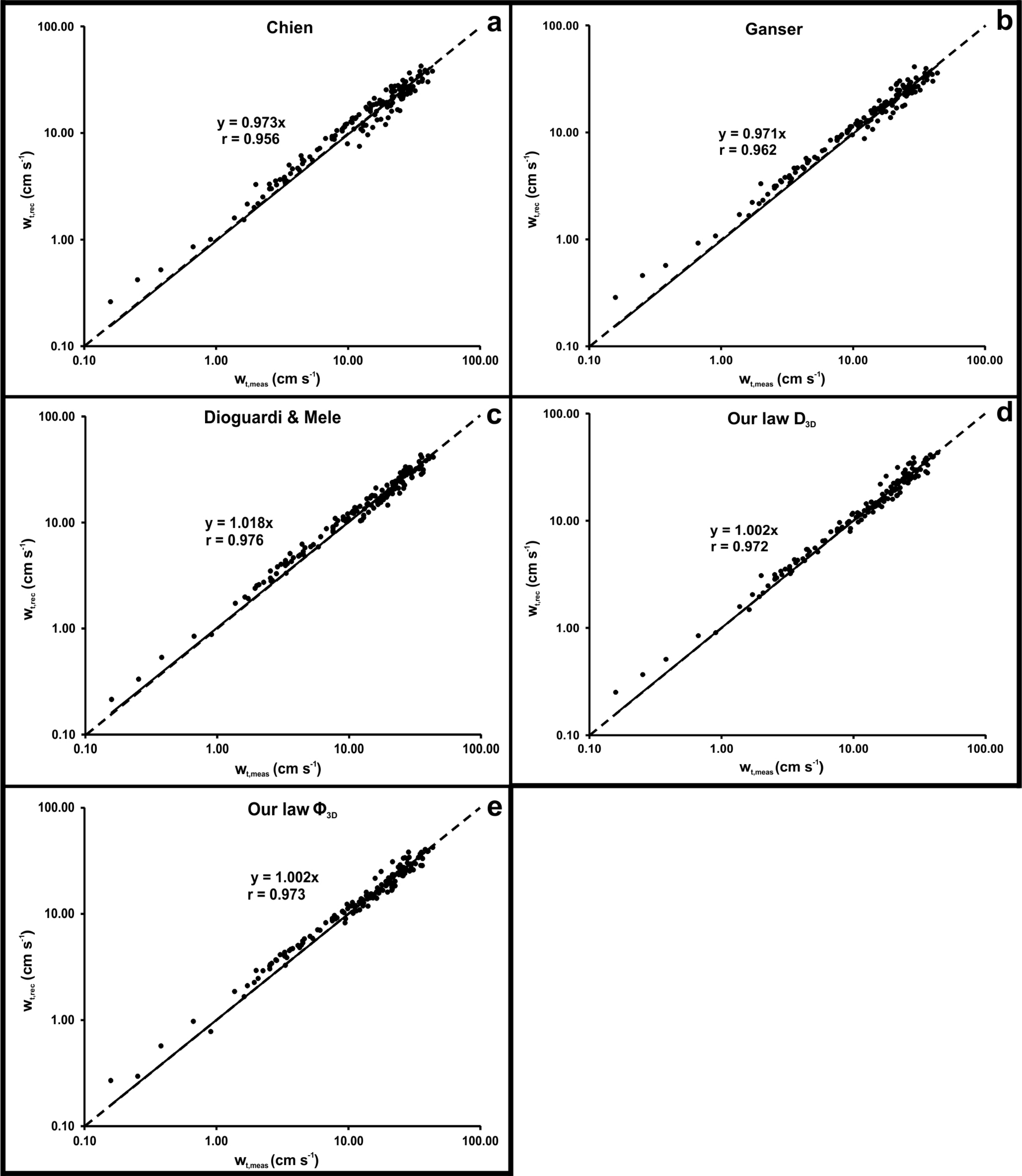
a
Chien
y = 0.973x
r = 0.956
b
Ganser
y = 0.971x
r = 0.962
c
Dioguardi & Mele
y = 1.018x
r = 0.976
d
Our law D3D
y = 1.002x
r = 0.972
e
Our law Φ3D
y = 1.002x
r = 0.973
wt,rec (cm s-1)
wt,meas (cm s-1)
0.10
1.00
10.00
100.00

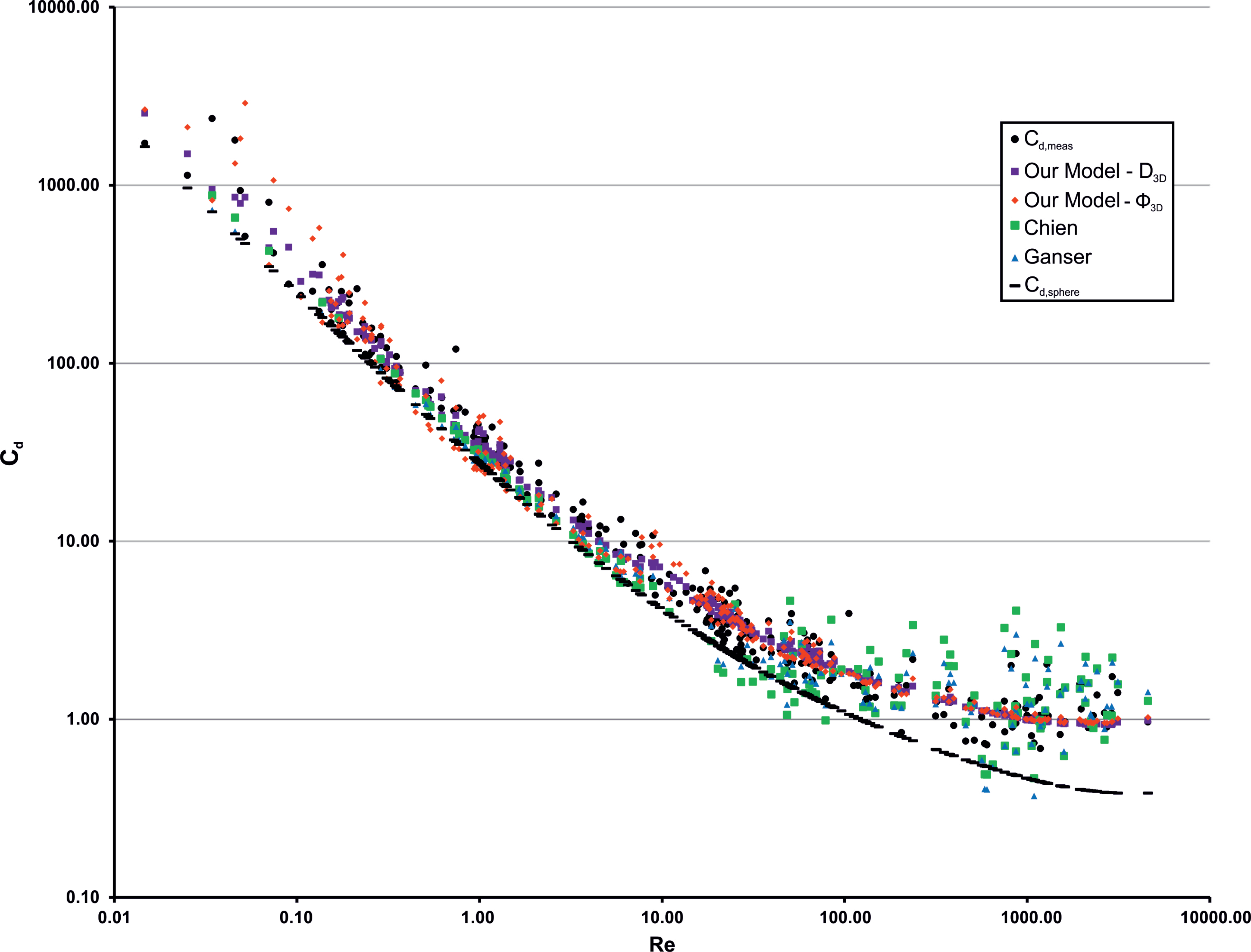

10000.00
1000.00
100.00
10.00
1.00
0.10
C_d
0.01
0.10
1.00
10.00
100.00
1000.00
10000.00
Re
C_d,meas
Our Model - D_3D
Our Model - Φ_3D
Chien
Ganser
C_d,sphere

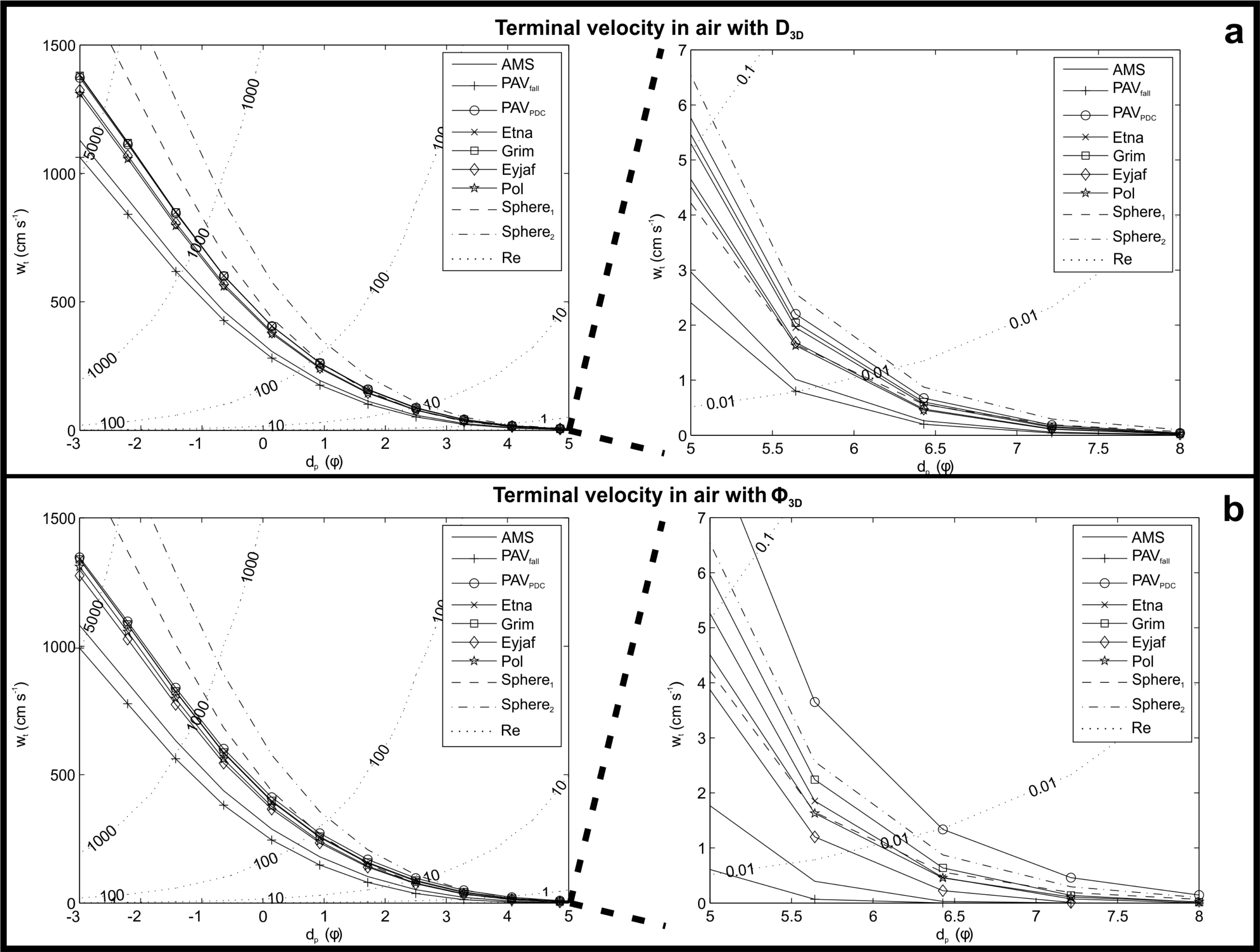

Terminal velocity in air with D_{3D}
a
Terminal velocity in air with Φ_{3D}
b
AMS
PAV_{fall}
PAV_{PDC}
Etna
Grim
Eyjaf
Pol
$Sphere_1$
$Sphere_2$
Re
w_t (cm s^{-1})
d_p (φ)